Nuclear Engineering and Design 335 (2018) 265–278

Contents lists available at ScienceDirect

Nuclear Engineering and Design

journal homepage: www.elsevier.com/locate/nucengdes

CFD simulation of the pre-heater of a nuclear facility steam generator using a thermal coupled model

Dario M. Godino*, Santiago F. Corzo, Norberto M. Nigro, Damian E. Ramajo

CIMEC Centro de Investigación de Métodos Computacionales, UNL, CONICET, FICH, Col. Ruta 168 s/n, Predio Conicet "Dr Alberto Cassano", 3000 Santa Fe, Argentina

A B S T R A C T

A thermal-hydraulic study of the pre-heater belonging to the steam generator of the nuclear experimental facility RD-14M was carried out. The thermal coupling between the primary and secondary flows was solved through three-dimensional Computational Fluid Dynamics (CFD) and the conjugated heat transfer model. The net heat transfer coefficient was calculated and compared with well-known literature correlations from Bell-Delaware and Kern, as well as with RELAP simulation. Acceptable agreement among the different methodologies was found, even though literature correlations underestimated heat transfer. The occurrence of flow stagnation, high turbulence, and recirculation zones in the secondary circuit was also analyzed. It was concluded that the Bell-Delaware correlation is suitable for preliminary calculus, and CFD is useful and reliable for designing as well as assessing heat transfer devices, giving a large understanding of the thermal hydraulic phenomena. Finally, the RELAP code showed to be fast and accurate to get the heat transfer and pressure loss with minimal input data requirements.

1. Introduction

The heat transfer between hydraulically isolated circuits is largely applied in many industrial applications such as steam generators (SG) of Nuclear Power Plants (NPP). Commonly, SG are tall vertical devices with thousands of U-tubes where a hot and pressurized primary fluid flows and transfers heat to a secondary fluid. The former is usually kept at a pressure lower than the primary fluid to promote evaporation. The steam generated in the U-tubes rises up toward the SG head dragging large amount of saturated water which is then separated by means of cyclones (MacDonald et al., 1996), and the remained moisture is removed by means of dryers later. Then, the water returns to the bottom of the SG through a downcomer, while the steam is driven to the turbine. That means that water recirculates inside the SG driven by density difference force until it is evaporated. Recirculation ratios ranging between 4 and 5 are usually found in this kind of SG. The SG is fill up by a feed-water flow, which can be pre-heated outside of the SG or inside it through a pre-heater.

Nowadays the main computational tools used for nuclear plants assessment are system codes such as RELAP (Dimenna et al., 1988), CATHENA (Hanna, 1998) and ATHLET (Lerchl and Austregesilo, 2003) among others. They allow solving the thermal hydraulics along the overall plant coupled with the in-core neutron flux and also accounting for the control and safety systems. This kind of codes is still the only feasible option to simulate long time transient events that involve the whole plant. However, despite of the good capabilities of system codes, they are worthless to simulate three-dimensional flows in complex geometrics. In these situations, additional information is often needed before assuming geometric or operative simplifications. Although the current computational resources are not large enough to simulate the whole NPP by 3D-CFD, the use of CFD to analyze specific components of NPP is growing up (Höhne et al., 2012; Corzo et al., 2015).

A well representation of the heat transfer phenomena in the core and also in the SG is crucial to know the NPP response. The different flow regimes, the mass change phenomena, and the geometry of the equipments entail a challenge for simulation. Therefore, today more attention is dedicated to improve the computational codes in order to better estimate the behavior of the active and passive safety systems under Design Basis Accidents (DBA) as well as severe accidents. On the one hand, single-phase heat transfer modeling has been largely studied. However, the solution of complex industrial geometries with turbulent flows should be dealt with carefully, because the results are largely depending on the mesh refinement and the turbulent model chosen. On the other hand, the available models for heat and mass transfer in two-phase flow should be enhanced to cover the range of operation conditions associated to nuclear installations.

* Corresponding author.
E-mail address: dmgodino@cimec.unl.edu.ar (D.M. Godino).
URL: http://www.cimec.org.ar (D.M. Godino).

https://doi.org/10.1016/j.nucengdes.2018.05.021
Received 4 December 2017; Received in revised form 2 May 2018; Accepted 17 May 2018

List of symbols

C_p	Heat capacity at constant pressure
D_i	Inner diameter of tubes
D_o	Outer diameter of tubes
e	Tube thickness
f	Friction factor
G	Mass flux
h	Heat transfer coefficient
k	Turbulent kinetic energy
K	Kinetic energy
L	Characteristic length
L_t	Tube length
$\dot{m}$	Mass flow rate
N	Amount of tubes
p	Pressure
pt	Tube pitch-to-diameter
q	Heat flux
t	Time
T	Temperature
$\widehat{H}$	Enthalpy
$\hat{u}$	Internal energy
ρ	Density
μ	Dynamic viscosity
μ_t	Turbulent viscosity
ν	Kinematic viscosity. ν_t Kinematic turbulent viscosity
ε	Turbulent dissipation rate
ω	Specific dissipation rate
τ	Viscous stress tensor.
τ_R	Reynolds stress tensor.
τ_t	Turbulent stress tensor.
κ	Thermal conductivity
$\mathbf{g}$	Gravitational acceleration
$\mathbf{U}$	Velocity
S	Strain rate tensor
$Re = \frac{UL}{\mu}$	Reynolds number
$Nu = \frac{hL}{\kappa}$	Nusselt number
$Pr = C_p\mu/\kappa$	Prandtl number

List of acronyms

CFD	Computational fluid dynamics
CHT	Conjugated heat transfer
GAMG	Geometric algebraic multi-grid
NPP	Nuclear power plant
PBICG	Preconditioned bi-conjugate gradient
PHWR	Pressure heavy water reactors
PWR	Pressurized water reactors
RANS	Reynolds-averaged Navier–Stokes
SG	Steam generator

Up to now, the SGs are still designed by means of empirical correlations, whose reliability is based on the use of conservative coefficients leading to the oversizing of the devices. However, in spite of the growing capabilities of CFD, it is becoming a choice for the designing stage.

There are a few works addressing simulations on shell tube with flower-shape baffles heat exchangers. One of the most valuable contributions is from You et al. (2012) who performed experimental tests as well as numerical simulations representing the tube bundle by means of a porous media with homogeneous losses. This methodology allows them to correlate the Reynolds number *Re* with the heat transfer coefficient *h*, the pressure loss, and also the velocity profile. The research from Wang et al. (2009), Taher et al. (2012) should be also remarked. They focused on the effect of different types of helical baffles, the baffle spacing, and the inclination. Ozden and Tari (2010) also studied the influence of the baffle spacing as well as the free passage area for different flows comparing CFD results against empirical correlations of Kern and Bell-Delaware. The above mentioned works aimed to the shell flow (secondary circuit) by assuming constant temperature at the tube walls. This assumption is quite right when overheated steam is flowing through the primary. However, it is not the scenario for the SG studied herein. Therefore, to solve the thermal coupling between primary and secondary flows should be advisable.

The state of the art regarding numerical simulation of thermal coupling between liquids and solid domains is scarce (Pairetti et al., 2013). In this sense the research works of Cong et al. (2013), Li et al. (2013) stood out. The first uses an explicit or weak coupling strategy and the former uses a more robust implicit methodology.

System codes, such as RELAP, take advantage of empirical correlations to solve the mass, momentum and energy balances within dimensionally reduced domains. As mentioned above, these codes are almost the only tool used in NPP simulation because they are capable to model different flow regimes (bubbly, slug, churn, annular, etc.) in combination with heat transfer modes such as laminar, turbulent, free convection, wall boiling, and critical heat flux, among others. However, to achieve the overall NPP model, some parameters which strongly depend on the geometry (friction an concentrated pressure drops, real heat transfer area), are replaced by arbitrary parameters in order to fit the global NPP variables such as the mass flow, the heat transfer, the pressure, and the temperature in steady state. Although the steady state solution could be acceptable, the model response under transient events may not be well represented.

In a previous research (Corzo et al., 2015), the current SG was studied in detail both with 3D-CFD and RELAP. In that case, the thermal coupling between the primary and secondary was not taken into account in the CFD model in order to focus the attention in the two-phase flow, the drag effects between phases, the recirculation ratio, and the pressure drop along the SG. Therefore, the heat transfer and the consequent boiling rate distribution were arbitrarily imposed, but the current work focuses on the single-phase thermo-hydraulics inside the pre-heater. This is the first step to achieve a complete model of the SG able to locally predict boiling. Due to experimental data of the pre-heater are unavailable, the comparison is carried out against empirical correlations and system code results.

The paper is organized as follow: in Section 2 the mathematical formulation of the governing equations is presented. Next, a detailed description of the Kern and Bell-Delaware empirical correlations, as long as the RELAP formulation is included. The geometrical and operational description of the pre-heater and the computational models is described in Section 3. Then, in Section 4 the simulation results are shown, analyzed and compared with the empirical methods. Finally the conclusions are outlined in the last section.

2. Mathematical formulation

2.1. Governing equations

The governing equations of the Conjugate Heat Transfer (*CHT*) model are from the *chtPimpleFoam* solver implemented in of the suite OpenFOAM©. Even though each one of the three domains (primary, solid and secondary) is solved implicitly, the *chtPimpleFoam* solves the couping explicitly in an iterative way, similar than a segregated solver. This coupling technique gives several advantages from the point of view of the computational implementation and leads to accurate solutions in

few iterations.

2.1.1. Fluid domains

The fluids flow is mathematically described by means of the Navier-Stokes equation along with the mass and energy conservation equations. This set of partial differential equations are assembly averaged (Favre average Favre, 1965) to reduce the spectra of spatial and temporal scales of the solutions. Finally, the resulting equations are written in terms of the independent variables (spatial coordinates and time) and the mean variables: pressure (p), internal energy ($\widehat{u}$) or the enthalpy ($\widehat{H} = \widehat{u} + \frac{p}{\rho}$), velocity ($\mathbf{U}$) and density ($\rho$). Then, the balance equations for Newtonian fluids with constant properties are expressed as follow:

- Mass balance:

$$\frac{\partial \rho}{\partial t} + \nabla\cdot(\rho\mathbf{U}) = 0 \tag{1}$$

- Momentum balance:

$$\frac{\partial(\rho\mathbf{U})}{\partial t} + \nabla\cdot(\rho\mathbf{U}\mathbf{U}) = -\nabla p + \nabla\cdot\tau_t + \rho g \tag{2}$$

- Energy balance:

$$\frac{\partial(\rho\widehat{u})}{\partial t} + \nabla\cdot(\rho\widehat{u}\mathbf{U}) + \frac{\partial(\rho K)}{\partial t} + \nabla\cdot(\rho K\mathbf{U}) = -\nabla\cdot q - \nabla\cdot(p\mathbf{U}) - \nabla\cdot(\tau_t\mathbf{U}) \tag{3}$$

where $\tau_t = \tau + \tau_R$ is the turbulent stress tensor, τ is the viscous stress tensor, and τ_R is the Reynolds stress tensor. Assuming that there is a relation (eddy viscosity hypothesis) between τ, τ^R and the mean velocity $\mathbf{U}$:

$$\tau_t = \mu_{eff}[\nabla\mathbf{U} + (\nabla\mathbf{U}^T)] - \frac{2}{3}\mu_{eff}(\nabla\cdot\mathbf{U})I \tag{4}$$

where $\mu_{eff} = \mu + \mu_t$ is the effective viscosity, μ is the dynamic viscosity and μ_t is the turbulent viscosity. I the identity tensor, K the kinetic energy, g the acceleration of gravity and κ the thermal conductivity.

By introducing the Fourier law, the conductive term in the energy equation takes the following form $q = -\kappa\nabla T$.

2.1.2. Turbulence model

Turbulence modeling is needed in both fluid domains. The pre-heater is in the end of the U-tube bundle. Therefore, the **primary flow** arriving to the pre-heater is fully developed and turbulent, hence the standard k-ε model (Launder and Spalding, 1974) with standard wall law is appropriated to close the equation system. k-ε solves two additional transport equations, one for the turbulent kinetic energy (k) (Eq. (5)) and the other for the turbulent dissipation rate (ε) (Eq. (6)).

$$\frac{\partial(\rho k)}{\partial t} + \nabla\cdot(\rho k\mathbf{U}) = \nabla\cdot\left(\frac{\mu_t}{\sigma_k}\nabla k\right) + 2\mu_t S{:}\,S - \rho\varepsilon \tag{5}$$

$$\frac{\partial(\rho\varepsilon)}{\partial t} + \nabla\cdot(\rho\varepsilon\mathbf{U}) = \nabla\cdot\left(\frac{\mu_t}{\sigma_\varepsilon}\nabla\varepsilon\right) + C_{1\varepsilon}\frac{\varepsilon}{k}\mu_t S{:}\,S - C_{2\varepsilon}\rho\frac{\varepsilon^2}{k} \tag{6}$$

Then, the turbulent viscosity is defined as follow:

$$\mu_t = \rho C_u\frac{k^2}{\varepsilon} \tag{7}$$

The model constants in Eqs. (5)–(7) are by default (Ferziger and Perić, 2002):

$C_u = 0.09$ $C_{1\varepsilon} = 1.44$ $C_{2\varepsilon} = 1.92$
$\sigma_k = 1.0$ $\sigma_\varepsilon = 1.3$

The **secondary flow** is quite more complex due to the following: the many sudden direction changes, the stagnation and recirculation zones, the detached flow at the baffles edges and around the tubes. Attending to that, a benchmark was solved in order to choose a suitable model and fulfill the mesh requirements. After carrying out a depth study over different models and grid refinements, the k-ω-SST model (Menter, 2906) was found to be quite suitable for this kind of flow. Details about this study are included in the results section. Hence, a brief view of the method is included. The k-ω-SST model also solves two transport equations: one for k (Eq. (8)) and the other for the specific dissipation rate (ω) (Eq. (9)).

$$\frac{\partial(\rho k)}{\partial t} + \nabla(\rho k\mathbf{U}) = \mu_t S{:}\,S - \beta^*k\rho\omega + \nabla\cdot((\mu + \sigma_k^*\mu_t)\nabla k) \tag{8}$$

$$\frac{\partial(\rho\omega)}{\partial t} + \nabla(\rho\omega\mathbf{U}) = \alpha\frac{\omega}{k}\mu_t S{:}\,S - \beta\rho\omega^2 + \nabla\cdot((\mu + \sigma_\omega\mu_t)\nabla\omega) \tag{9}$$

where μ_t is defined as $\mu_t = \rho k/\omega$.

The model coefficients and auxiliary relations are by default (Moukalled et al., 2015):

$\alpha = 0.555$ $\beta = 0.075$ $\beta^* = 0.09$
$\sigma_k^* = 0.5$ $\sigma_w = 0.5$ $\varepsilon = \beta^*\omega k$

2.1.3. Solid domain

In this case, only the thermal equation is solved and the resulting equation is accomplished from the energy balance and the Fourier law:

$$\frac{\partial(\rho_s C_p T)}{\partial t} = \nabla\cdot(\kappa_s\nabla T) \tag{10}$$

where κ_s, ρ_s and C_p are the thermal conductivity, density and heat capacity of the solid.

2.2. Empirical methods

In this section the most widely employed empirical correlations to calculate heat transfer and pressure loss in heat exchangers are presented.

The current pre-heater is a semi cylindrical-shape heat exchanger. Hence, the available correlations, usually found for typical heat exchangers, have to be modified attending to this particular case.

2.2.1. Heat transfer

The empirical methods estimate the heat transferred Q through the net heat convective coefficient (h) and the heat transfer area A:

$$Q = hA\Delta T \tag{11}$$

where ΔT is the average temperature difference between the primary and secondary flows. In the next subsection the correlations for each of the two fluid domains are introduced.

Inside of U-tubes the widely known empirical correlation of Dittus-Boelter (Dittus and Boelter, 1985) is employed:

$$Nu_t = \frac{h_t D_i}{k} = 0.023Re^{0.8}Pr^n \tag{12}$$

$0.6 \leqslant Pr \leqslant 160$
$Re \geqslant 10000$
$\frac{L}{D_i} \geqslant 10$

where Nu and Pr are the Nusselt and Prandtl numbers, respectively. h_t is the convective coefficient of the inner side of the tube and D_i and L are the inner diameter and the length of the tube. Finally, the exponent n takes different values depending on the heat direction ($n = 0.3$ if the fluid is being cooled and $n = 0.4$ if fluid is being heated).

In the secondary domain the correlations have to account for the by-pass losses due to flow passing around the tube bundle (named by-pass

flow) and due to the flow crossing through the baffle-shell gaps (named by-pass baffle-shell) and through the baffle-tube gaps (named by-pass baffle-tube) (Cao, 2008). The present paper describes the correlations from Kern (1974) and Bell-Delaware Kakaç et al. (1981), which allow estimating both the thermal transfer coefficient and the pressure loss. It must be remarked that the Kern correlation is too conservative, and consequently, only advisable in preliminary analysis. On the other hand, the Bell-Delaware method takes into account some additional effects, such as the three above mentioned by-pass losses, leading to more accurate estimations.

The Kern correlation reads:

$$h_{o,c} = \frac{k}{D_o} 0.36 Re_s^{0.55} Pr_s^{0.33} \left(\frac{\mu_w}{\mu_b}\right)^{0.14} \tag{13}$$

where μ_w is the viscosity evaluated at the tube wall temperature T_w, μ_b is the viscosity in the bulk and D_o is the outer diameter of the tube. This correlation is able for baffles with open areas (pitch area) lower than 25%. However, the open area of the currently studied pre-heater is around 40%.

On the other hand, the Bell-Delaware correlation includes the by-pass flow effects:

$$h_{o,c} = \left[jCp_{sec} G_{sec} Pr_{sec}^{-2/3} \frac{\mu_w}{\mu_b}^{0.14} \right] \left[\frac{\phi \xi_h}{X} \frac{h_L}{h_{NL}} \right] \tag{14}$$

where Cp_{sec} and G_{sec} are the heat capacity and the mass flux of the secondary fluid, j is the Colburn coefficient, ϕ is a correction factor to adjust the ideal tube banks result by considering the window effects, ξ_h is a loss correction factor per by-pass flow, X is a correction factor to account for the amount of tubes fully crossed by the flow (the tubes that no cross the baffle window). Finally, the ratio h_L/h_{NL} accounts for the shell-tubes and baffles-tube losses. The last was neglected because gaps were not considered in the CFD model.

2.2.2. Pressure loss correlations

The pressure loss of the primary circuit ΔP_p was estimated using the Fanning expression, adopting a friction factor f in function of the Re:

$$\Delta P_p = 4fN \frac{L_t}{D_i} \frac{G_p^2}{2\rho} \left(\frac{\mu_w}{\mu_b}\right)^a \tag{15}$$

where the exponent a is -0.14 and -0.25 for laminar and turbulent flow, respectively. L_t is the length of one tube, N the amount of tubes, and G_p is the mass flux in the primary circuit.

There are several methods to estimate the pressure loss in the secondary circuit ΔP_s, although some of them are unsuitable for certain geometries (Cao, 2008). The Kern method should not be applied for heat exchangers with large number of steps or large leakage gaps. On the other hand, the Bell-Delaware method is valid in these cases, and the expression is:

$$\Delta P_s = 2\Delta P_{BP} \left(1 + \frac{N_w}{N_c}\right) + (N_B - 1)\Delta P_{BP} + N_B \Delta P_w \left(\frac{\Delta P_L}{\Delta P_{NL}}\right) \tag{16}$$

In Eq. (16) the first term on the right corresponds to the inlet and outlet losses. The second term accounts for the cross flow and the last term corresponds to the baffles windows. ΔP_{BP} is the loss of an ideal tube bundle corrected by leakage or by-pass flow, ΔP_w is the loss in the windows, N_c is the amount of tube rows that never cross any window, N_w is the amount of tube rows that cross the baffle windows and N_b is the amount of baffles. Finally, the term $\Delta P_w/\Delta P_{NL}$ is a leak correction factor, which is equal to unity if leakage is neglected. ΔP_{BP} and ΔP_w are defined as follows:

$$\Delta P_{BP} = \frac{4fN_c G_s^2}{2\rho_w} \left(\frac{\mu_w}{\mu_b}\right)^{0.14} \tag{17}$$

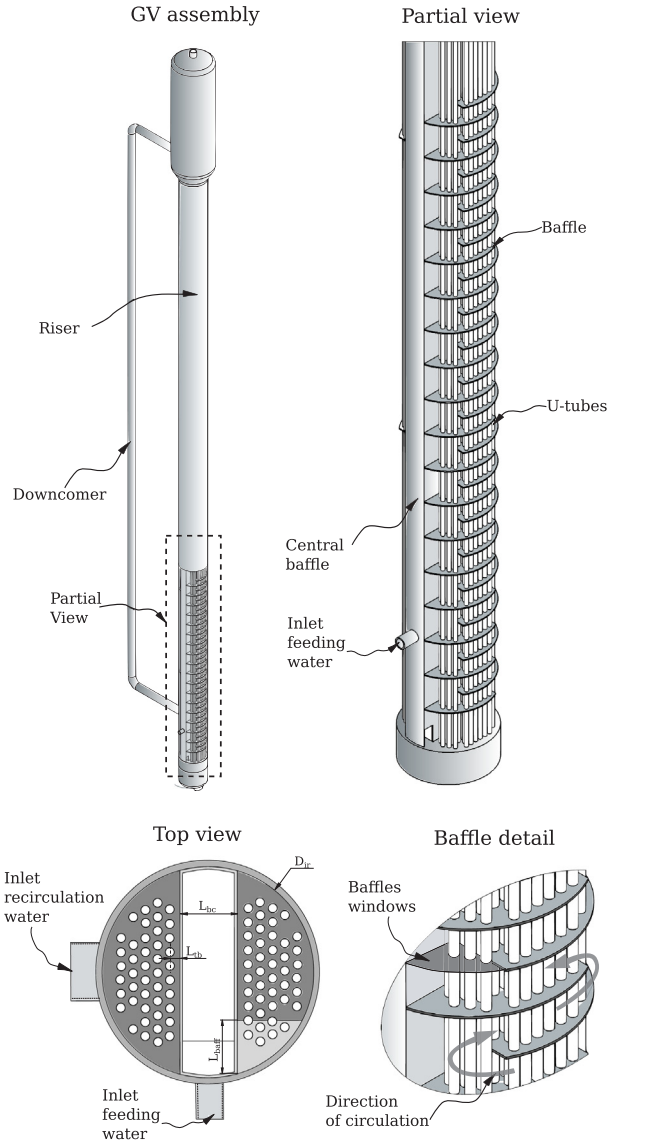

Fig. 1. Views of the steam generator and details of the pre-heater.

$$\Delta P_w = (2 + 0.6N_w) \frac{\rho_w V_z^2}{2} \xi_{\Delta P} \tag{18}$$

where V_z is the superficial velocity in the window, which is calculated as $V_z = \dot{m}/(\rho\sqrt{S_s S_w})$, with $\dot{m}$ the mass flow rate and S_s and S_w the cross-flow area and the window area, respectively. Finally, $\xi_{\Delta P} = e^{-\alpha_r F_{BP}}$ is a by-pass correction factor, where $\alpha_r = 4$ is a coefficient that depends on the flow regime and F_{BP} is the by-pass fraction.

3. Computational model

The studied steam generator is a component of the experimental facility RD-14M, which was built to assess the Pressurized Heavy water reactor (PHWR) CANDU 6. The main objective was to study Loss Of Coolant Accidents (LOCA). Therefore, relevant data regarding pressure loss, temperature, or heat transfer inside the pre-heater of the SG are unavailable.

The Fig. 1 shows the SG geometry. The U-tube bundle is housed in a vertical cylindrical tube called riser, which is split in two legs by means of a vertical bane. One leg receives the saturated re-circulated water coming from the downcomer (external pipe), whereas the other leg contains the pre-heater in its bottom side. The pre-heater receives the cold feed-water.

Despite the fact that the overall pre-heater has 26 steps, only two steps were simulated (Fig. 2). This allowed refining the mesh enough to obtain a detailed representation of the geometry. The computational model was composed of three regions:

- **Primary circuit:** the bundle of 44 tubes through which the coolant water flows down from the top to the bottom. The inlet condition was a total mass flow of 24 kg/s at 10 MPa and 584 K.
- **Secondary circuit:** The semicircular domain bounded by the riser and the vertical bane through which the secondary water flows up from the bottom to the top. The inlet condition was a total mass flow of 2 kg/s at 4.5 MPa and 460 K.
- **Tubes:** The solid tubes which conduct the heat between the **primary** and **secondary circuits**. The rest of the solids (baffles, shell and bane) was assumed as walls without thickness and adiabatic. The material of the tubes was Incoloy-800 (κ = 16.3 W/mK).

Due to the direction of the primary flow, the tubes were extended upstream to ensure fully developed flow at the pre-heater inlet.

Constant fluid properties were considered both to performing the CFD as well as the empirical correlation calculus. The Table 1 summarizes the constructive and operation parameters of the model.

3.1. 3D OpenFOAM model

The three domains were discretized using extruded grids. The surfaces were meshed with 2,175,036 triangular and quadrangular elements while the volume was meshed with 39,665,600 pentahedra and hexahedra. The mesh close to the wall was as fine as required to achieve y^+ values in accordance to the previous test results. Mesh details are shown in Fig. 3. High refinement both at the inner and outer tube walls was required to correctly capture the heat transfer.

Due to the pseudo-stationary nature of the solutions, time averaged solutions from transient runs were preferred. An adjustable time step with a maximum Courant number of 1.5 was chosen. The limit was always reached in the primary domain while the Courant in the secondary domain remained lower than 0.6. The three domains were thermally-coupled by using the *CHT* solver, which is based on the combination of the solvers *heatConductionFoam* and *buoyantFoam* for conjugating the heat transfer between the solid and fluid regions. The solver employs an iterative method to find the temperatures shared by neighbor regions.

The solver uses the PIMPLE method for the pressure-velocity coupling. Within each PIMPLE loop a PISO loop is solved updating the temperature of the fluid and the solids. In those surfaces shared by two regions, the boundary condition derives from the adjacent region. Thus, when the PIMPLE loop converges, the temperature on the shared surface should be the same for the two regions.

To achieve acceptable convergence, two inner and two outer PIMPLE corrections were performed. Regards the linear solver algorithm, a Geometric Algebraic Multi-Grid (GAMG) was selected to solve the pressure equation and the Preconditioned Bi-Conjugate Gradient (PBICG) was chosen for the rest of the equations. The tolerance criteria for the linear solver was an absolute residual of 10^{-6}, or a relative residual of 10^{-3}. First order was used for divergence terms, linear schemes for the laplacian and gradient terms, and Backward Euler for the temporal integration.

The run was performed in parallel, with a distributed memory arquitecture using 24 processors (E5-1660-v3, 26 GB-RAM DDR3, 160GBHD, Infiniband QDR4 Gbps). Some variables such as the average temperature of the secondary fluid (T_{2s}) and the heat flux at the tubes surface (q_s) were monitored to evaluate the convergence of the solution. Once the monitors stabilized, the simulations were continued to get time-averaged field solutions. Approximately 72 h of simulation were required to perform the runs.

3.2. System code model

System code simulations were performed using RELAPMod3, which is one of the most widespread used codes for nuclear engineering. The mathematical and physical background is reported in depth in the code manual (Carlson et al., 1990; Shieh et al., 2014) and several publications and technical reports (Končar and Mavko, 2003; Ransom and Mousseau, 1991; Mousavian et al., 2004). Therefore, only a brief overview of the heat transfer modeling is included in the current section.

Fig. 4 shows the model of the overall steam generator performed in a previous work (Corzo et al., 2017). In the same figure could be seen highlighted the current model extracted from the original one.

Depending on the nature of the flow, the RELAP code has three heat transfer models called flag 101, 110 and 111, which are suitable for parallel flow, cross-flow, and tube bundles with cross-flow, respectively. The code uses different correlations for each case. In Fig. 4 different colors were used to identify the four heat structures required for the overall steam generator. The HS were discretized following the hydraulic nodalization in the stream flow direction, while four nodes in the transversal direction were considered. The default *HS* model for parallel flow (Geometry flag 101) was implemented in all cases with the exception of *HS*1, which corresponds to the pre-heater. For this, the vertical tube bundle with cross-flow (Geometry flag 110) model was set in order to improve the heat transfer.

The algorithm implemented in RELAP for the heat transfer estimation is very reliable and robust. This allows handling many kinds of geometries and flow regimes. The calculation starts by determining the flow regime and the thermodynamic condition inside each cell by means of an integer coefficient (Wall convection heat transfer mode number, ht), which can take values between 0 and 12. e.g., $ht = 1$ for single-phase liquid, $ht = 2$ for sub-cooled wall with $\alpha < 0.1$, $ht = 4$ for saturated nucleate boiling, $ht = 7$ for sub-cooled film boiling, and $ht = 11$ for condensation in steam, among others. Then, depending on *ht* and the heat structure (101, 110 or 111), the code chooses among the different correlations, e.g., the flow in the pre-heater is single-phase and sub-cooled in both the primary and secondary circuits. Therefore, ht = 2.

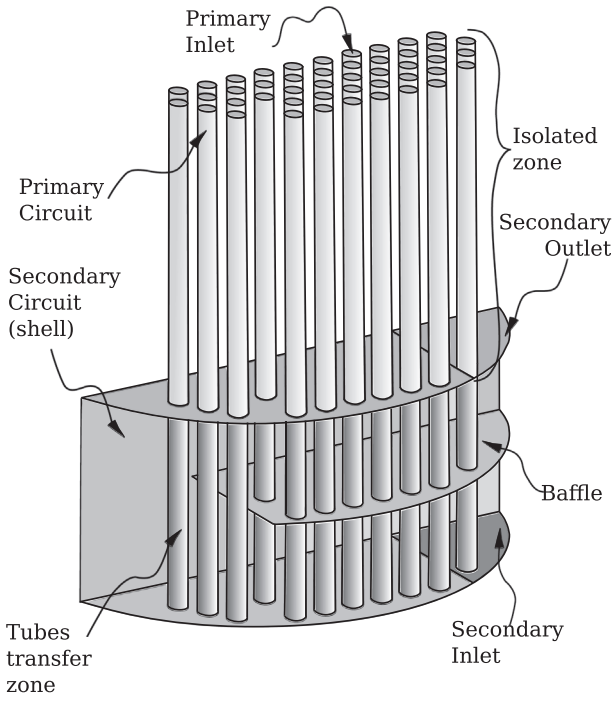

Fig. 2. Computational domains.

Table 1
Constructive and operational parameters of the pre-heater. *See Fig. 1 for reference.

Primary circuit – Tubes	
Primary mass flow $\dot{m}_p$	24 kg/s
Temperature at Inlet T_{ip}	585 K
Amount of tubes N	44
Tube outer diameter D_0	15.88 mm
Tube length L_t	155.6 mm
Distance between tube centers Pt	24 mm
Pressure P_p	10 MPa
Water heat capacity Cp_p	6143 J/kgK
Secondary circuit – Shell	
Secondary mass flow $\dot{m}_s$	2 kg/s
Temperature at Inlet T_{is}	460 K
Distance between baffles	77.8 mm
Pressure P_s	4.5 MPa
Water heat capacity Cp_s	4866 J/kgK
Riser inner diameter D_{ir}	363 mm
Distance baffle to tube L_{tb}*	22.5 mm
Central bane width L_{bc}*	95 mm
Baffle window width L_{baff}*	91.1 mm
Solid region – Tubes	
Tube thickness e	1.13 mm
Thermal conductivity k_{so}	16.3 J/kgK

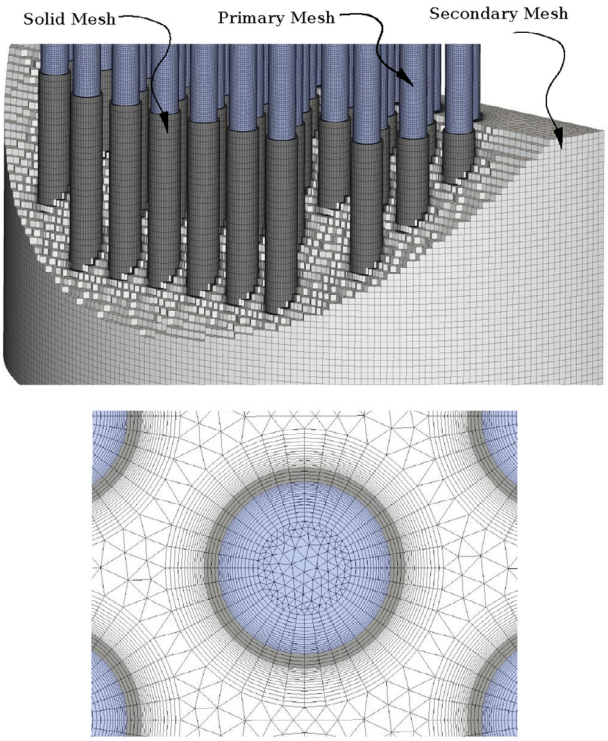

Fig. 3. Views of the mesh.

For the primary circuit, the *parallel flow* heat structure (101) computes an effective heat transfer coefficient (h_{eff}) by taking the maximum of three *Nu*:

$$h_{eff} = \frac{\kappa}{D} max(Nu_{free}, Nu_{lam}, Nu_{turb}) \tag{19}$$

where Nu_{lam} is for laminar flow. In this case, the Sellars constant value (Sellars et al., 1954) is adopted ($Nu_{lam} = 4.36$). The Nu_{free} corresponds to free convection flow, and it is estimated from the Churchill-Chu correlation for vertical tubes(Churchill and Chu, 1975), and from McAdams (1954) for horizontal tubes. Finally, the Nu_{turb} estimation is accomplished by the widely used Dittus-Boelter correlation before introduced (12). It was found out that the Nu_{turb} was the largest of the three.

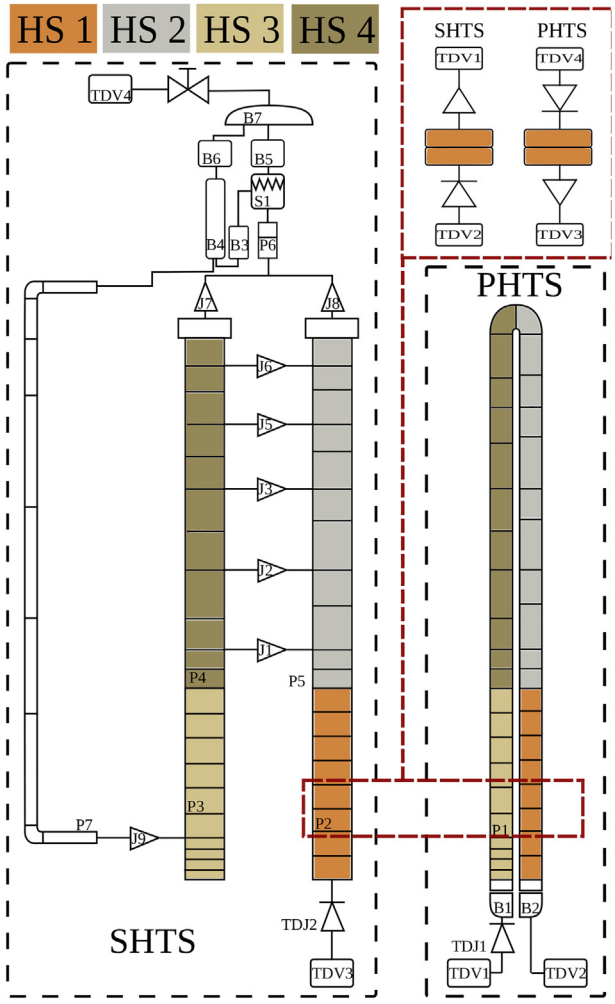

Fig. 4. Nodalization of the SG and PH in RELAP.

For the secondary flow, the correlation for *vertical bundles parallel flow* heat structure (110) differs from heat structure 101 only in the introduction of a turbulent flow multiplier developed by Inayatov (1975), which substitutes the Dittus-Boelter coefficient for a C_{bund} coefficient, which takes into account the pitch to diameter ratio (P_t/D_o):

$$C_{bund} = 0.023 \frac{P_t}{D_0} \tag{20}$$

RELAP limits the maximum and minimum pitch to diameter ratio (P_t/D_o) to 1.6 and 1.0, respectively. For the pre-heater the distance between the tube centers (P_t) is 24 mm and $P_t/D_o = 1.5$.

If the cross flow is also activated (*HS* 111), the effective heat transfer coefficient h_{eff} accounts for both as follows (Kutateladze, 1961):

$$h_{eff} = (h_{par}{}^2 + h_{cross}^2)^{0.5} \tag{21}$$

where h_{par} represents the parallel heat transfer referred as *HS* 101 or 110. The cross flow coefficient h_{cross} is computed using the Shah correlation (Shah, 1992):

$$Nu = 0.21 \left(G_{cross} \frac{D_0}{\mu} \right)^{0.62} Pr^n \tag{22}$$

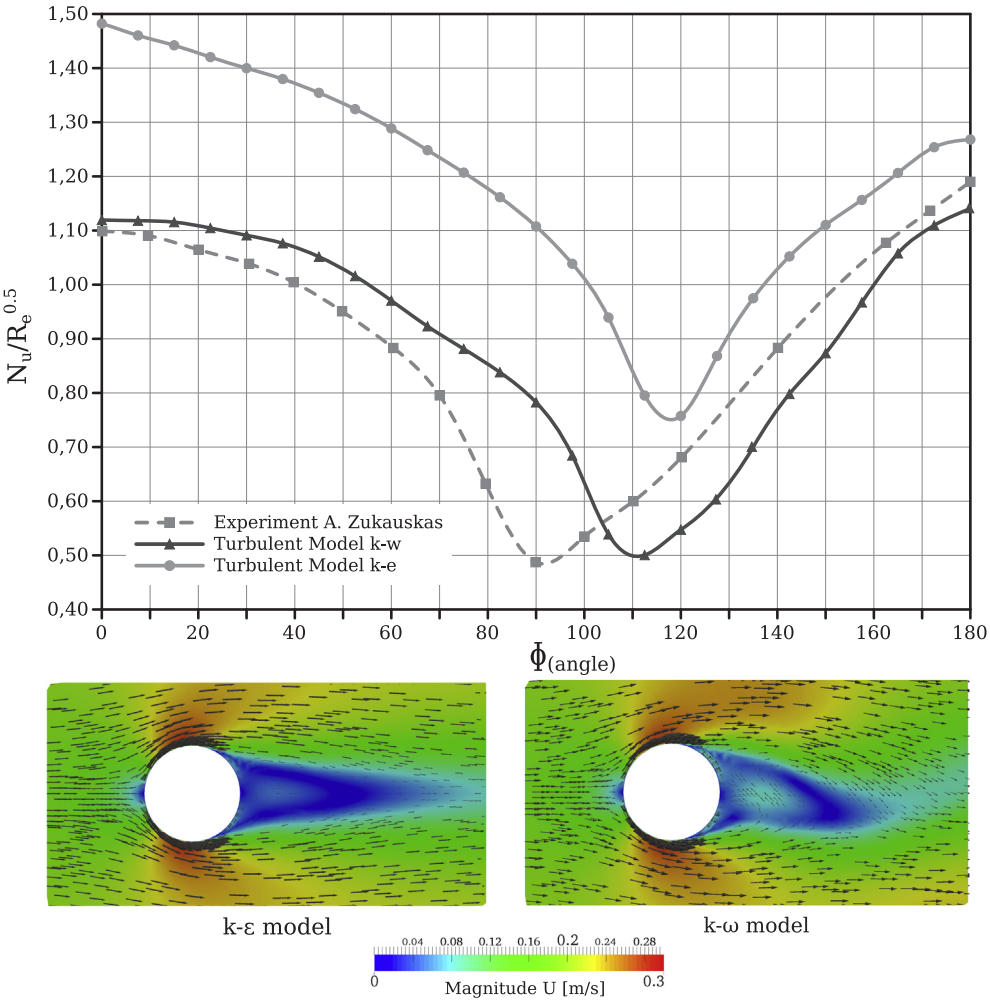

Fig. 5. Validation test – Re = 25,000 (mesh 4).

Table 2
Validation of turbulence models.

Model	Nu	Error	C_D	Error
Experiment (Žukauskas, 1972)	138	–	1.150	–
$k-\omega$ model	141.33	0.61%	1.142	0.7%
$k-\varepsilon$ model	186.59	34.70%	1.012	12.0%

where G_{cross} is the cross mass flux. This heat structure can only be used if the associated hydraulic components have mass fluxes in at least two of the three coordinate directions (x, y, z),.g, if the tubes bundle is aligned with the x-coordinate, the parallel and cross mass fluxes are $G_{par} = G_x$ and $G_{cross} = A_{ratio} *(G_y^2 + (G_z^2)^{1/2}$, respectively. The coefficient A_{ratio} introduced in the G_{cross} expression accounts for the real cross area of the flow:

$$A_{ratio} = \frac{1-\frac{\pi}{4}\frac{D}{P^2}}{1-\frac{D}{P^2}} \tag{23}$$

Despite the availability of the *HS* 111 in RELAP, the setting was completely unclear for us due to the necessity of defining the hydraulic components in two dimensions. Added to this, the cross transversal flow area varies due to the semi-circular sheet shape, thus introducing a variable flow area. In order to overcome those problems, we decided to use a parallel vertical bundle heat structure (*HS* 110), and to represent the secondary circuit as a tube with a total length calculated as the zig-zag path length, keeping the tube true height, though. The former was in order to account for the larger heat transfer area due to zig-zag path.

Table 3
Convergence of mesh – 48 circumferential cell.

Parameters	Experimento	Mesh 1A	Mesh 2A	Mesh 3A	Mesh 4A	Mesh 5A	Mesh 6A	Mesh 7A
$N_{radialcells}$	–	3	5	8	11	14	17	20
$y+_{average}$	–	14.340	8.876	4.813	3.358	2.295	1.610	1.147
Cd	1.150	0.825	0.869	0.956	1.142	1.198	1.325	1.351
$Error_{Cd}$	–	28.3%	24.4%	16.9%	0.7%	4.17	15.30	17.49
Nu	138.00	106.92	120.44	131.27	138.84	136.06	128.68	122.17
$Error_{Nu}$	–	22.5%	12.7%	4.9%	0.6%	1.40	6.75	11.47
Detachment	89.90	127.50	122.20	120.00	112.50	105.1	97.49	93.12
$Error_{Detach}$	–	41.8%	35.9%	33.5%	25.1%	16.9%	8.4%	3.6%

Table 4
Convergence of mesh – 80 and 120 circumferential cell.

Parameters	Experiment	Mesh 5B	Mesh 6B	Mesh 7B	Mesh 8B	Mesh 9B	Mesh 10B	Mesh 7C
$N_{radialcells}$	–	14	17	20	23	26	29	20
$y+_{average}$	–	2.224	1.562	1.121	0.822	0.642	0.515	1.092
Cd	1.150	1.222	1.248	1.211	1.195	1.189	1.185	1.201
$Error_{Cd}$	–	6.2%	8.5%	5.3%	3.9%	3.4%	3.0%	4.43
Nu	138.00	132.42	128.40	124.54	122.55	121.50	121.21	125.04
$Error_{Nu}$	–	4.0%	7.0%	9.8%	11.2%	12.0%	12.2%	9.38%
$Detach$	89.90	94.05	90.00	90.00	90.00	90.00	90.01	90.01
$Error_{Detachment}$	–	4.6%	0.1%	0.1%	0.1%	0.1%	0.1%	0.1

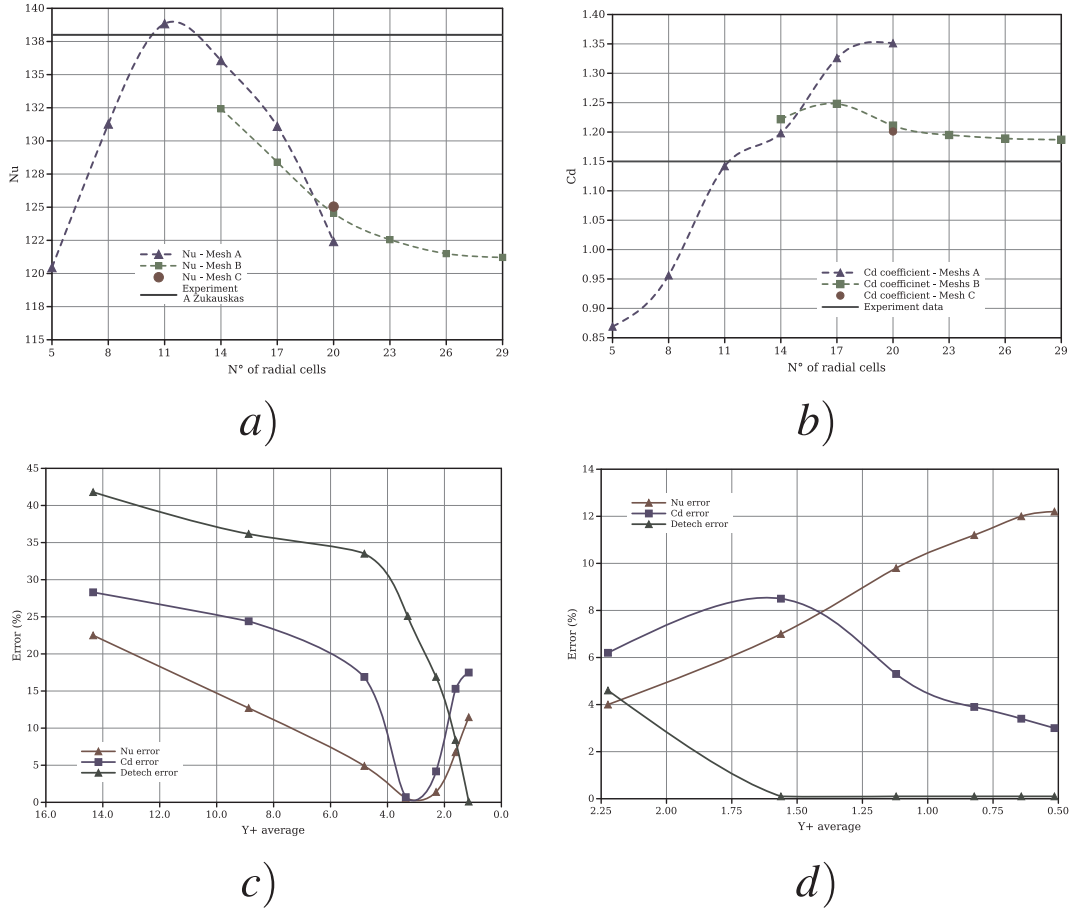

Fig. 6. Mesh convergence results: a) Nusselt number, b) Drag, respect the amount of cells and Error for: c) Mesh A, d) Mesh B respect the $y+$ parameter.

4. Results and discussion

In this section, the CFD results are presented and compared with the empirical estimations and RELAP results. The comparison is especially focused on the effective heat transfer and the pressure drop.

To ensure a right setting of the physical models and mesh parameters, a benchmark simulation was achieved by CFD before solving the pre-heater.

4.1. Benchmark: Heat transfer and drag force around a cylinder

The turbulence modeling and the near wall refinement are largely known to have a significant effect on the heat transfer and pressure loss. These issues represent a challenge in CFD. In order to find the better relationship between accuracy and computational requirement, an experimental test performed by Žukauskas (1972) was reproduced by CFD. The test consisted in water flowing around a cylinder with constant wall temperature. From the large amount of experimental data, the $Re = 25,000$ case was chosen because of its similarity with the pre-heater flow. The two more employed turbulence models for industrial applications, $k-\varepsilon$ and $SST-k-\omega$, were analyzed, and the grid dependence was also investigated. For the former, 3D extruded grids with layering refinement in the radial direction close to the cylinder were implemented. The effect of the azimuthal refinement was also assessed.

The analysis was carried out in two steps. Firstly, the turbulence models were assessed with a given mesh. Secondly, for the most proper turbulence model, a complete mesh convergence study was accomplished.

4.1.1. Turbulence modeling

Fig. 5 on the top shows the parameter $Nu/Re^{0.5}$ around the cylinder for both turbulence models. Results were obtained with a fine grid with a local refinement of 11 layers around the cylinder. As showed in the figure, the heat transfer was largely overestimated by $k-\varepsilon$ model all around the cylinder, and especially in the front zone (0°). The global error with $k-\varepsilon$ grew up to 34.7%. On the other hand, the SST-$k-\omega$

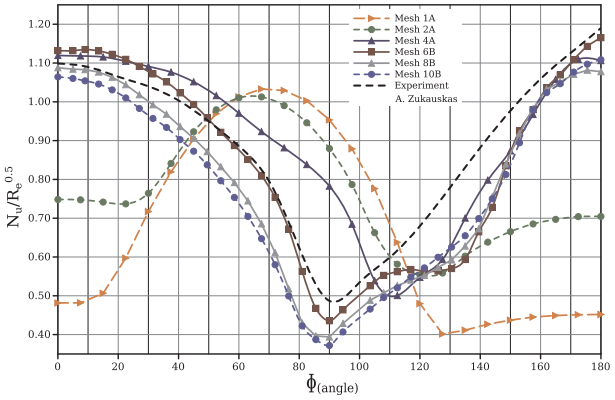

(a) Convergence of Nusselt

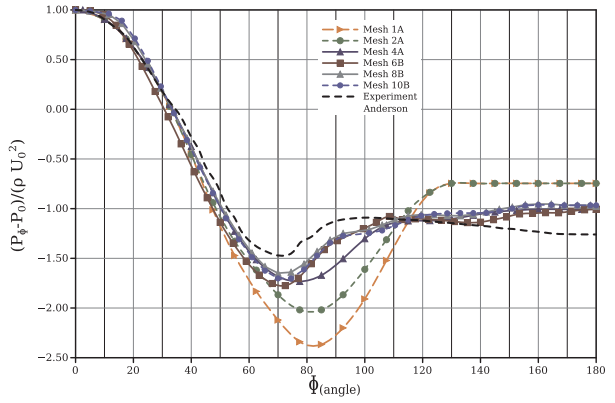

(b) Convergence of normalized pressure

Fig. 7. Variation angular – Convergence Mesh.

Table 5
Temperature boundary conditions for the empirical correlations.

Temperature K	Primary	Secondary
Inlet	T_{iP} = 565.0	T_{iS} = 460.0
Outlet	T_{oP} = 563.9	T_{oS} = 472.8
Tube Wall	T_{wP} = 553.4	T_{wS} = 523.0
Bulk	T_{bP} = 565.0	T_{bS} = 470.9

estimations were much better with the experimental data in the whole locations, and consequently the global error was the lowest.

The results presented in the current study are in accordance with the literature. In most of the cases, the $k-\varepsilon$ model throws poor results in complex flows involving severe pressure gradient, separation flow and strong streamline curvature. However, the k-ω-SST model is more suitable for complex boundary layer flows under adverse pressure gradients and separated flows.

The position where the flow was detached from the cylinder was badly estimated by both models, although SST-$k-\omega$ was better. The SST-$k-\omega$ model captured the detached point 20° after the experimental position, whereas the discrepancy reached up to 30° with the $k-\varepsilon$ model. The maximum *Nu* took place just at the back of the cylinder (80°), because the detachment of turbulent structures increased the heat transfer. It can be concluded that $k-\varepsilon$ overestimated the heat transfer over all the cylinder, while the $k-\omega$ gave relatively good estimations, being the maximum error at 90°.

Fig. 5 at the bottom shows the velocity magnitude for both models. As expected, $k-\varepsilon$ gave diffusive solutions, and vortexes detaching cannot be identified. On the other hand, SST-$k-\omega$ captured the detaching, characterizing the typical solutions of this kind of external turbulent flows.

The total *Nu* and the drag coefficient C_D are shown in Table 2 along with their respective errors. As above mentioned, SST-$k-\omega$ gave very low errors about 0.61% and 0.7% for *Nu* and C_D, respectively. On the other hand, $k-\varepsilon$ largely overestimated the heat transfer and the global error grew up to 34.7%, although the drag error was lower (12%).

4.1.2. Mesh requirements

Mesh refining was performed both in the radial and azimuthal directions. The radial mesh was assessed increasing the amount of layers in the first millimeter from the wall, while three sets of azimuthal refinements were accomplished. They were named A, B, and C, corresponding to 48, 80 and 120 cells in the azimuthal direction. That is equal to 7.5°, 4.5°, and 3°, respectively. Tables 3 and 4 show the parameters of the meshes studied along with the *Nu* and C_D results and the corresponding errors. The angle for detaching was also included. As the tables show, the radial refinement was increased to the extent that the azimuthal refinement was increased too. For the finest mesh (120 cells) only one radial refinement was assessed (20 cells in radial direction). In both tables, the numbers (1–10) in the label "Mesh" represent the radial refinement level, and the letters A, B and C represent the different azimuthal refinements.

Fig. 6 summarizes the mesh convergence results. In Fig. 6a and b, the blue line corresponds to A-mesh group (48 cell in azimuthal direction), the green line corresponds to B-mesh group (80 cells), and the red point corresponds to the only one C-mesh. The experimental data was also included as a horizontal black line. In Fig. 6c and d, the relative errors with respect to the experimental data are drew as a function of the average y^+ parameter. Fig. 6c corresponds to A-mesh group and Fig. 6d to the C-mesh group. As displayed, for A-meshes both the drag (C_D) and the heat flux (*Nu*) progressively converged to reach errors of 0.7% and 0.6%, respectively. However, if y^+ is reduced below 4.0 the errors quickly increased. On the other hand, for B-meshes the C_D continued even more by reducing y^+, although *Nu* grew up. That means that the aspect ratio of the nearest elements also had a significant influence on convergence. Therefore, it can be inferred that the used wall law is not suitable for y^+ lower than a certain value with also depends on the aspect ratio of the layers. However, the use of azimuthal refinement such as the used for B-mesh group allows obtaining grid convergence by refining in the radial direction. This did not mean that the error decreed, but it reached a constant value. Finally, the only one point simulated with mesh-C showed slightly differences with respect to the B-mesh case (the enhancement was lower than 1%). Then it was

Table 6
Heat Transfer Coefficient H.

Analysis method	Heat Flux W	Heat Transfer Coefficient			Difference
		Primary side W/m^{2}K	Secondary side W/m^{2}K	Global W/m^{2}K	% with Bell-Delaware
CFD	144196	42444	6701	4234	5.20
RELAP	123100	36075	6648	3809	5.38
Bell-Delaware	134678	40913	6231	4025	–
Kern	130721	40913	5952	3907	2.94

Table 7
Primary and secondary load loss.

Analysis	Secondary load loss Pa				Primary load loss Pa	
method	In baffle	Cross-Flow	Total	Difference %	In tubes	Difference %
CFD	392	2118	2510	7.32	1457.6	0.3
RELAP	–	–	2500	6.89	1400	4.24
Bell-Delaware	395.3	1943.5	2338.8	–	1462	–

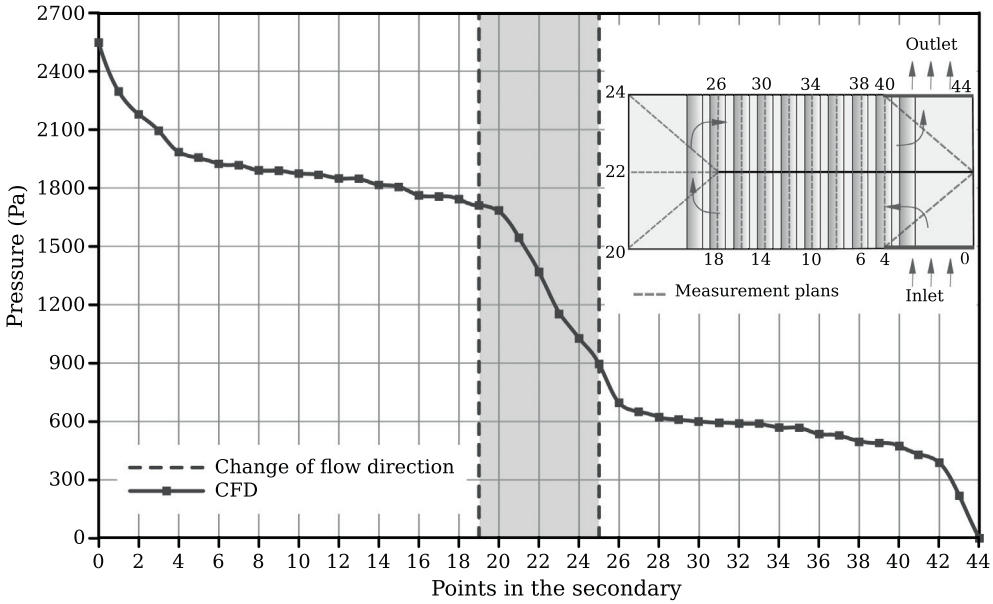

Fig. 8. Secondary pressure distribution.

concluded that the b-mesh azimuthal refinement was enough. As for the detachment point, it presented a rapid convergence for the whole groups of meshes, reaching really small errors (lower than 0.1%).

The $Nu/Re^{0.5}$ distribution in function of the angle was also analyzed. As shown in Fig. 7a, for the two coarser meshes (meshes 1A-2A) the results were fairly different to the experimental data, especially at the front and back of the cylinder. This could be caused by the excessive numerical diffusion introduced by the mesh. On the other hand, from the grid refinement mesh 3A, the results improved considerably and the global error was significantly reduced, but the detachment point was underpredicted. This mesh was able to capture the vortexes detachment and the consequent oscillatory phenomena that toke place behind the cylinder. As above mentioned, the detachment point was adequately captured by the B-meshes.

Fig. 7a shows how the heat transfer distribution progressively enhanced and fit the experimental data for the whole range of angles while also the average Nu approached better the global results. The refinement improves the total heat transfer, the local distribution, and the angular location of detaching.

Fig. 7b displays the pressure distribution around the tube. Here again the coarser meshes led to very unaccurated estimations, whereas cases 4-A and 6B–10B showed similar behaviors, thus demonstrating a convergent tendency.

The agreement reached in the mean C_D and its distribution, added to the right distribution obtained for the Nu, led to infer that the difference observed for the whole heat flux could be explained by differences in the thermal properties between the experimental test and the CFD simulations. Other possibility could be found in the large sensitivity of some turbulent parameters such as the turbulent Prandlt number (Pr_t).

Based on the benchmark results, it is concluded that SST-$k-\omega$ combined with a mesh refinement similar to mesh 4 is suitable for solving the thermal–hydraulic of the pre-heater, thus allowing obtaining certain estimations of the heat transfer as well as the pressure drop.

4.2. Pre-heater model

The inlet conditions for the primary and secondary circuits were fixed to apply the empirical methods, and the output conditions were obtain from the CFD results. Then, in order to get the total heat transfer Q from Eq. (11), a characteristic temperature was calculated as the logarithmic mean temperature difference:

$$T_{LMTD} = \frac{(T_{iP}-T_{oS})-(T_{oP}-T_{iS})}{ln(T_{iP}-T_{oS})/(T_{oP}-T_{iS}))} \quad (24)$$

This is a usual assumption in heat exchanger design and it is valid when the heat transfer coefficient is assumed constant in the whole device.

Table 5 shows the set of temperatures used.

Table 6 shows the heat transfer coefficient h obtained by the different methods. Differences of 5.38% and 5.20% were observed by comparing the RELAP and CFD results against the Bell-Delaware one. This agreement can not be considered as a validation of the computational methods, although it gives more certainty about their capability for solving this kind of devices, which involve complex thermal and fluid dynamic phenomena.

Table 7 shows the pressure drops in the primary and secondary circuits. There was agreement between the pressure drop estimations from the different methods. The different percentages were also calculated with reference to the Bell-Delaware method. In the secondary circuit, the CFD results accounted for the pressure drops by cross-flow and by the direction change of the flow at the baffle edges. The differences obtained between CFD, RELAP and the Bell-Delaware method

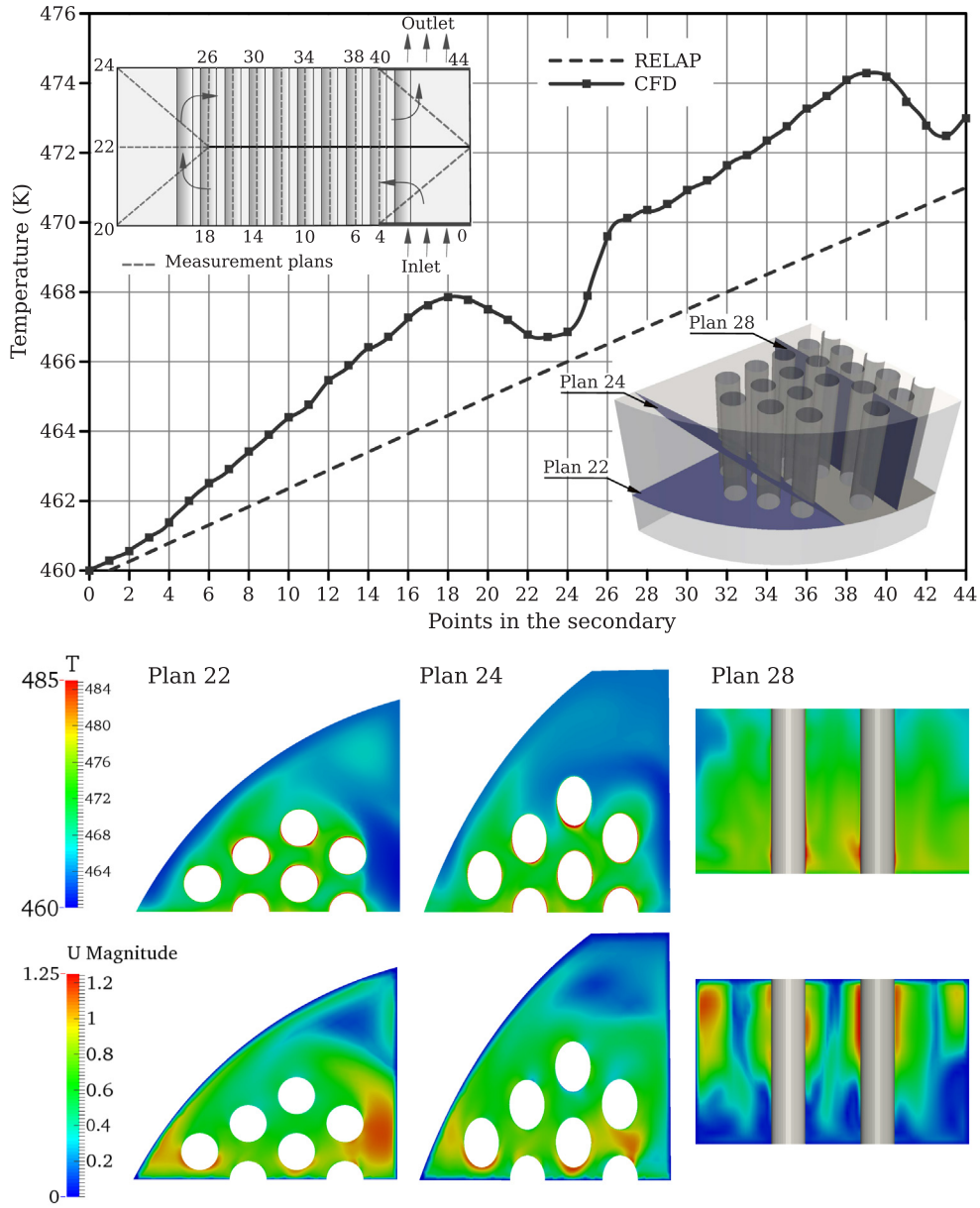

Fig. 9. Temperature in the secondary domain. Top: Temperature distribution along a pathline. Bottom: Contours of temperature in some cut planes.

were of 7.32% and 6.89%, respectively. On the other hand, for the primary circuit the differences were of 0.3% and 4.24%, respectively. This small differences were expected because the pressure drop in internal fully-developed flows in tubes is a well-known problem. On the contrary, the larger differences in the secondary circuit reflected the higher difficulty to calculate the flow through the tubes and the baffle windows, where it was highly turbulent and non-steady. Despite these difficulties, the current results are acceptable for engineering applications.

Fig. 8 shows the pressure drop along a pathline in the secondary domain. The vertical gray band is indicating the change of direction through the baffle window. Each point in the curve was got as the area-average pressure over a plane perpendicular to the pathline (see the scheme on the top right side in the figure). As noted, the pressure strongly fell down in the baffle window (around 30% of the total pressure drop) because of the area narrowing and the flow direction change. This remarks the biggest weakness of the Kern method, which only considers the bundle cross-flow. A similar behavior was found in the inlet and outlet regions. In these cases, the pressure showed an asymmetric distribution that allows to conclude that the total pressure drop along the 26 steps of the overall pre-heater could be inferred from the results of the current partial model.

The area-average temperature profile along the pathline is shown in Fig. 9. In this case, the RELAP results were also included. Due to the geometrical simplifications performed in the RELAP model, the results showed a linear distribution. On the other hand, from CFD simulation a more complex profile was observed although a quasi-linear behavior across the bundle zone was found. As noted, the CFD predicted a higher temperature at the output (1.5 K).

Large reductions in the area-average temperature distribution were found around the windows, the inlet, and outlet regions. As can be seen in the pictures at the bottom (Planes 22, 24 and 28), these temperature drops are explained by the existence of large zones with low temperature and low velocity close to the corners and the shell wall. In Fig. 10, the temperature and velocity patterns in four horizontal planes (see the sketch at the bottom of the figure) are displayed. As it is displayed in the figure, the velocity changed significantly for the different planes.

Due to the lower resistance, the flow passed easily around the tube

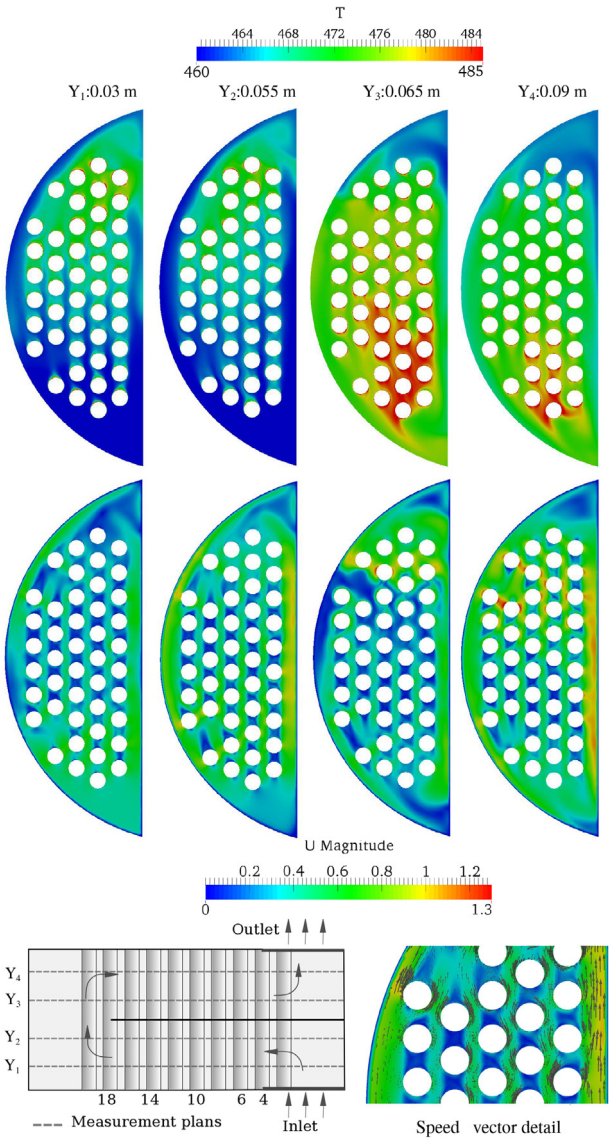

Fig. 10. Velocity and temperature in horizontal planes.

bundle (by-pass flow), and consequently a low temperature close to the shell was evidenced. This effect is displayed in Fig. 10 in planes Y_1 and Y_2. As noted, the fluid near the shell and the central bane remained cold until arriving to the baffle window. When this cold stream mixed with the hot stream that crossed the bundle at the window, the area-average temperature fell down, as is evidenced in Fig. 9.

It can be remarked the high temperature difference between the planes Y_2 and Y_3, in part caused by considering the baffle as adiabatic. It is also remarkable the large hot spot observed in plane Y_3, and to a lower extent in plane Y_4. Due to the sudden direction changes, the flow tended to lean against the upper walls, thus reducing the velocity near the bottom walls.

By comparing the velocities in the four planes, it can be concluded that the two first ones had a quite laminar and more structured flow pattern inside the bundle. The influence of one tube over the next one was significant, which is evidenced by the low velocity regions joining two adjacent tubes. On the other hand, in planes Y_3 and Y_4 the flow seems to be more turbulent and vortex detachment can be visualized behind some tubes.

In order to have a better understanding of the thermal patterns in the secondary side, the axial temperature profile over the wall of one tube located in the central zone of the bundle is presented in Fig. 11.

The analysis was performed over four vertical lines as shown at the bottom. It should be remarked that line *A* faces the flow in the first step of the pre-heater, but it is at the back in the second step.

The temperature distributions of the four lines presented a similar behavior from a macroscopic point of view. A large stratification along the axial direction was observed inside each step. Moreover, in a given height the temperature jumped between two adjacent lines reaching up to 15 K. As it was before mentioned, in both steps the flow leaned over the upper side, thus cooling the top part of the tube. On the contrary, at the bottom side of both steps, the lower velocity and the recirculation led to a lower heat transfer and the tube temperature remained hotter.

Note that the temperature profiles in both steps were not as similar as expected. Differences could be due to the uniform velocity imposed at the inlet. Therefore, Periodic boundary conditions should be more appropriated.

Even though the leakage flow through the tube to baffle gaps was not taken into account and the thermal conduction through the baffle was avoided, it is expected that the temperature difference along the axial and azimuthal directions in tubes would be significant. Therefore, this kind of studies should be of especial attention to perform stress calculus induced by thermal dilatation. The usefulness of these results shows the potentiality of CFD over the other methods.

The picture at the bottom right side in Fig. 10 shows the velocity vectors around the tubes. The flow pattern was the expected for an infinite arrangement of aligned tubes. Although the mesh was not enough fine to visualize the detachment of vortexes, the low velocity and the wake behind the tubes were clearly evidenced. That was in accordance with the results obtained for the single-tube test (see Fig. 5), for which the stagnation zone behind the tube extended down-stream for more than 1.5 diameters.

In order to study the temperature inside the tubes, a cut plane sectioning three tubes in the secondary step is shown in Fig. 12. Tubes N1 and N2 belong to the row nearest the central bane, and tube N3 is inside the bundle. The velocity vectors around the tubes are also displayed in the figure. The flow around tube N3 was the expected inside an aligned infinite array, thus causing an almost symmetric temperature distribution. The azimuthal temperature distribution was similar than the above studied for the benchmark case (see the Nusselt number distribution in Fig. 7a). The largest heat transfer took place at the front zone. Then, it progressively decreased until reaching a minimum value around the detachment point. In contrast with the observed for the single tube in the benchmark, in tube N3 the heat transfer did not increased behind the tube because the surrounding tubes avoided or disturbed the recirculation that enhanced the heat transfer at the back of the tube.

On the other hand, the flow around tubes N1 and N2 was strongly influenced by the flow passing between the bundle and the central bane wall. The largest asymmetry in the velocity field was found in tube N2, and it impacted on the lower temperature found at the right side of the tube. As noted, the tubes were cooled at the front, but the temperature remained higher at the back zone. The difference between the temperatures at the inner and the outer tube walls reached up to $30K$.

As expected, the highest thermal gradient was in accordance with the highest flow velocities and with the coolest temperatures in the solid tubes. The location of the detachment point could be found by examining the change in the temperature in the outer side of the tubes. That is, the detaching coincided with the point where the temperature grew up.

Although this paper is focused on the heat transfer between the two fluid domains, it is clear that the temperature gradients in the three directions (axial, azimuthal and radial) could have a strong effect on the mechanical stresses caused by thermal expansion. By combining the axial and azimuthal temperature profiles shown in Fig. 11 and the radial temperature maps of Fig. 12, it can be inferred that the solid tubes are subject to large temperature gradients. It should be remarked that the temperature maps inside the solid tubes are only possible thanks to

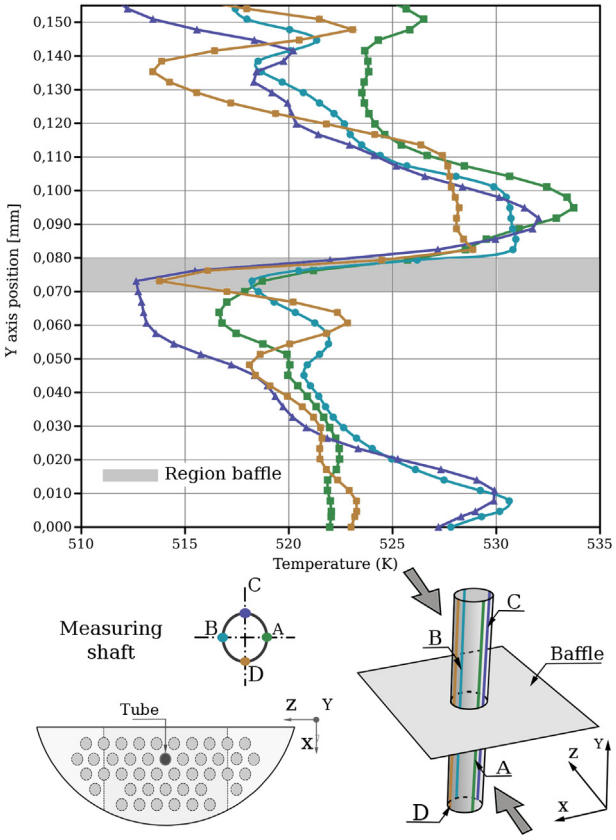

Fig. 11. Axial temperature in tubes.

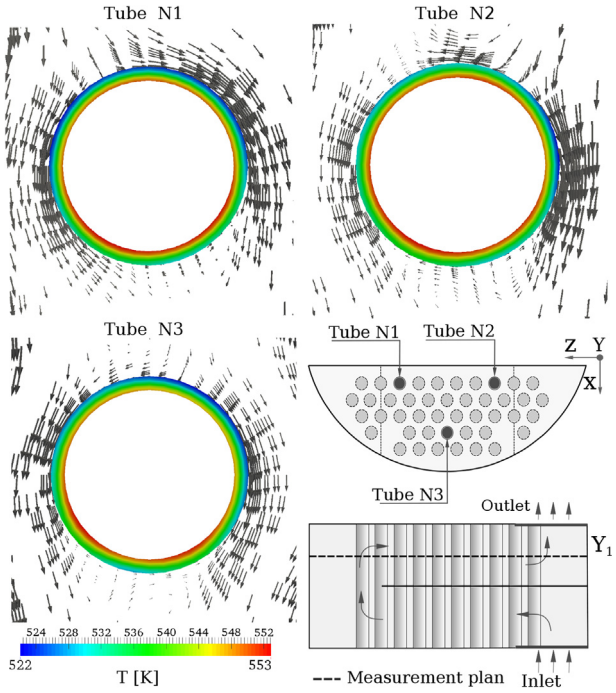

Fig. 12. Temperature distribution in the solid.

the use of the *CHT* model.

Fig. 13 on the top shows the streamlines of flow colored by the fluid temperature, whereas the y^+ parameter over the tube walls is displayed in the picture at the bottom. The streamlines point out some of the aspects about the flow distribution before discussed: the uniformity of the flow in the first step of the pre-heater, the detachment of vortexes

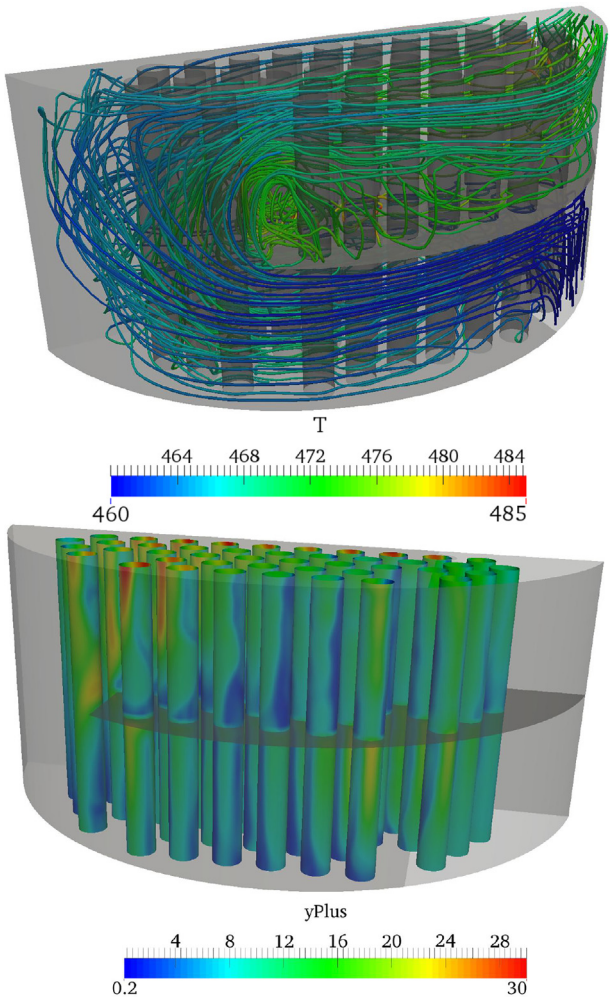

Fig. 13. Top: Streamlines. Bottom: y^+.

around the baffle edge, and the way the flow lean against the upper wall in both steps. Although the velocity over the tube walls is null by the non-slip condition, the y^+ displayed in the picture at the bottom is a proper indicator of the velocity near the tubes. As noted, velocities are higher in the surface of the tubes hit by the flow. In these zones y^+ grew up to 20. However, the maximums were found after the flow turned round at the window and hit the upper part of the tubes. In this case, the y^+ increased up to 35. Despite the local increments, the average y^+ is around 5.0. The agreement between the CFD and Bell-Delaware correlation for heat transfer was possible due to the radial refinement of the mesh at both sides of the tubes. By comparing the average y^+ with those reported for the benchmark test in Table 4, it is possible to infer that the overall errors in the heat transfer coefficient and pressure drop should be around 5% and 13%, respectively.

Two important aspects of the design of the heat exchangers are the spacing between baffles and the tube pitch area. The currently studied pre-heater fulfill the optimum constructive parameters recommended by Ozden and Tari (2010). However, the CFD results suggested that the narrowing in the flow induced by the recirculation after the baffle edge could be partially mitigated by adding some flow deflectors.

5. Conclusions

CFD allowed to obtain valuable qualitative and quantitative information about the thermal hydraulic phenomena in a true complex geometry.

It was possible to visualize the flow patterns, recirculation,

narrowing zones, and high temperature regions over the tubes. It was also possible to calculate the global heat transfer and the pressure loss. CFD results were compared with well-known empirical correlations and RELAP simulations, founding accordance among them. The Bell-Delaware correlation and the RELAP model were found suitable tools to perform initial estimations. Both shown to be more conservative than the CFD model.

The CHT model implemented in OpenFOAM© was robust and reliable allowing calculating the heat transferred between the two hydraulic circuits as well as the temperature across the tube thickness. Thanks to that, the high temperature gradients in the axial, radial and azimuthal directions were calculated. These results have a crucial importance for performing the calculation of mechanical stress caused by thermal expansion.

Acknowledgements

The authors would like to thank Universidad Nacional del Litoral (CAI+D 2016 PIC 50420150100067LI) and Agencia Nacional de Promocion Cientifica y Tecnologica (PICT 2016-2908).

Appendix A. Supplementary data

Supplementary data associated with this article can be found, in the online version, athttp://dx.doi.org/10.1016/j.nucengdes.2018.05.021.

References

Cao, E., 2008. Transferencia de Calor en Ingeniería de Procesos. Nueva Libreria.
Carlson, K., et al., 1990. RELAP/MOD3 Code Manual. US Nuclear Regulatory Commission.
Churchill, S.W., Chu, H.H., 1975. Correlating equations for laminar and turbulent free convection from a vertical plate. Int. J. Heat Mass Transfer 18 (11), 1323–1329.
Cong, T., Tian, W., Qiu, S., Su, G., 2013. Study on secondary side flow of steam generator with coupled heat transfer from primary to secondary side. Appl. Therm. Eng. 61 (2), 519–530.
Corzo, S., Ramajo, D., Nigro, N., 2015. 1/3d modeling of the core coolant circuit of a phwr nuclear power plant. Ann. Nucl. Energy 83, 386–397.
Corzo, S.F., Godino, D.M., Nigro, N.M., Ramajo, D.E., 2017. Thermal hydraulics simulation of the RD-14M steam generator facility. Ann. Nucl. Energy 105, 282–301.
Dimenna, R., Larson, J., Johnson, R., Larson, T., Miller, C., Streit, J., Hanson, R., Kiser, D., 1988. RELAP5/MOD2 models and correlations. Nuclear Regulatory Commission, Washington, DC (USA).
Dittus, F., Boelter, L., 1985. Heat transfer in automobile radiators of the tubular type. Int. Commun. Heat Mass Transfer 12 (1), 3–22.
Favre, A., 1965. Equations des gaz turbulents compressibles. 2. methode des vitesses moyennes methode des vitesses macroscopiques ponderees par la masse volumique. J. Mec. 4 (4), 391.
Ferziger, J.H., Perić, M., 2002. Computatational Methods of Fluid Dynmics, volume 3 Springer, Berlin.
Hanna, B., 1998. Cathena: a thermalhydraulic code for candu analysis. Nucl. Eng. Des. 180 (2), 113–131.
Höhne, T., Apanasevich, P., Lucas, D., Vallée, C., Beyer, M., et al., 2012. Application of a new drag coefficient model at cfd-simulations on free surface flows relevant for the nuclear reactor safety analysis. Ann. Nucl. Energy 39 (1), 70–82.
Inayatov, A.Y., 1975. Correlation of data on heat transfer flow parallel to tube bundles at relative tube pitches of 1.1 s/d 1.6. Heat Transfer-Soviet Res. 7 (3), 84–88.
Kakaç, S., Bergles, A., Mayinger, F., Heat exchangers: thermal-hydraulic fundamentals and design. Advanced Study Institute book. Hemisphere Pub. Corp., 1981.
Kern, D.D., 1974. Process Heat Transfer, vol. 1 McGraw Hill, New York (NY).
Končar, B., Mavko, B., 2003. Modelling of low-pressure subcooled flow boiling using the relap5 code. Nucl. Eng. Des. 220 (3), 255–273.
Kutateladze, S., 1961. Boiling heat transfer. Int. J. Heat Mass Transf. 4, 31–45.
Launder, B.E., Spalding, D.B., 1974. The numerical computation of turbulent flows. Comput. Methods Appl. Mech. Eng. 3 (2), 269–289.
Lerchl, G., Austregesilo, H., 2003. Athlet mod2 cycle a. User's Manual, GRS.
Li, Y., Yang, Y., Sun, B., 2013. Numerical investigation of thermal–hydraulic characteristics in a steam generator using a coupled primary and secondary side heat transfer model. Ann. Nucl. Energy 55, 258–264.
MacDonald, P., Shah, V., Ward, L., Ellison, P., 1996. Steam generator tube failures. US Nuclear Regulatory Commission, Washington, DC, Report No. NUREG/CR-6365.
McAdams, W.H., Heat transmission. Technical report, 1954.
Menter, F., Zonal two equation kw turbulence models for aerodynamic flows. In: 23rd fluid dynamics, plasmadynamics, and lasers conference, page 2906, 1993.
Moukalled, F., Mangani, L., Darwish, M., 2015. The finite volume method in computational fluid dynamics: an advanced introduction with OpenFOAM and Matlab, vol. 113. Springer, 2015.
Mousavian, S., Misale, M., D'Auria, F., Salehi, M., 2004. Transient and stability analysis in single-phase natural circulation. Ann. Nucl. Energy 31 (10), 1177–1198.
Ozden, E., Tari, I., 2010. Shell side CFD analysis of a small shell-and-tube heat exchanger. Energy Convers. Manage. 51 (5), 1004–1014.
Pairetti, C.I., Aguerre, H.J., Nigro, N.M., 2013. Mecánica computacional. Heat Mass Transfer (b) 33, 3379–3398.
Ransom, V., Mousseau, V., Convergence and accuracy of the relap5 two-phase flow model. In: Proceedings of the ANS International Topical Meeting on Advances in Mathematics, Computations, and Reactor Physics, 1991.
Sellars, J.R., Tribus, M., Klein, J., Heat transfer to laminar flow in a round tube or flat conduit: the graetz probem extended. 1954.
Shah, M., 1992. Heat transfer and fluid flow data books. Genium Publishing, Section 507, 7.
Shieh, A., Ramsom, V., Krishnamurty, R., Relap5/mod3 code manual, volume 6: Validation of numerical techniques. Informe Técnico NUREG/CR-5535/Rev, 3.
Taher, F.N., Movassag, S.Z., Razmi, K., Azar, R.T., 2012. Baffle space impact on the performance of helical baffle shell and tube heat exchangers. Appl. Therm. Eng. 44, 143–149.
Wang, Q., Chen, Q., Chen, G., Zeng, M., 2009. Numerical investigation on combined multiple shell-pass shell-and-tube heat exchanger with continuous helical baffles. Int. J. Heat Mass Transf. 52 (5), 1214–1222.
You, Y., Fan, A., Huang, S., Liu, W., 2012. Numerical modeling and experimental validation of heat transfer and flow resistance on the shell side of a shell-and-tube heat exchanger with flower baffles. Int. J. Heat Mass Transf. 55 (25), 7561–7569.
Žukauskas, A., 1972. Heat transfer from tubes in crossflow. Adv. Heat Transfer 8, 93–160.